Exchange-biased hybrid gamma-Fe2O3/NiO core-shell nanostructures

He, Xue-Min; Zhang, Chuang-Wei; Guo, Fang-Fang; Yan, Shi-Ming; Li, Yong-Tao; Liu, Li-Qing; Zhang, Hong-Guang; Du, You-Wei; Zhong, Wei

Published in:
Physical Chemistry Chemical Physics

DOI:
10.1039/c9cp01265f

Publication date:
2019

PCCP

PAPER

View Article Online
View Journal | View Issue

Cite this: *Phys. Chem. Chem. Phys.*, 2019, **21**, 11967

Exchange-biased hybrid γ-Fe_2O_3/NiO core–shell nanostructures: three-step synthesis, microstructure, and magnetic properties†

Xue-Min He,[ab] Chuang-Wei Zhang,[a] Fang-Fang Guo,[c] Shi-Ming Yan,[d] Yong-Tao Li,*[a] Li-Qing Liu,[a] Hong-Guang Zhang,[a] You-Wei Du[b] and Wei Zhong*[b]

Received 5th March 2019,
Accepted 7th May 2019

DOI: 10.1039/c9cp01265f

rsc.li/pccp

A two-step solvothermal method combining a calcination process was conducted to synthesize γ-Fe_2O_3/NiO core–shell nanostructures with controlled microstructure. The formation mechanism of this binary system has been discussed, and the influence of microstructures on magnetic properties has been analyzed in detail. Microstructural characterizations reveal that the NiO shells consisted of many irregular nanosheets with disordered orientations and monocrystalline structures, packed on the surface of the γ-Fe_2O_3 microspheres. Both the grain size and NiO content of nanostructures increase with the increasing calcination temperature from 300 °C to 400 °C, accompanied by an enhancement of the compactness of NiO shells. Magnetic studies indicate that their magnetic properties are determined by four factors: the size effect, NiO phase content, interface microstructure, *i.e.* contact mode, area, roughness and compactness, and FM–AFM (where FM and AFM denote the ferromagnetic γ-Fe_2O_3 and the antiferromagnetic NiO components, respectively) coupling effect. At 5 K, the γ-Fe_2O_3/NiO core–shell nanostructures display certain exchange bias (H_E = 60 Oe) and enhanced coercivity (H_C = 213 Oe).

Introduction

The exchange bias (EB) effect is classically manifested as the coupling interaction across interfaces between ferromagnetic (FM) and antiferromagnetic (AFM) components,[1] which have been widely investigated for their essential physical mechanism[2,3] and applied in various attractive fields, such as spin valves,[4] ultra-high density data storage,[5] magnetic tunnel junctions[6] and spintronic devices.[7] As observed in the experiments, the main indication of EB behavior is the shift of the hysteresis loop along the field axis after field cooling from above the Néel temperature (TN) of the AFM materials in FM/AFM systems.[8] Up to now, the EB effect and related phenomena have been reported in nanostructured systems including lithographically fabricated nanostructures,[9] chemically modified nanoparticle surfaces,[10] FM nanoparticles embedded in AFM matrices,[11] and controlled core–shell nanostructures,[12] *etc.* A core–shell EB system consisting of transition metals and their oxides, for example, Co/CoO[13,14] and Ni/NiO[15,16] core–shell nanoparticles, has particularly attracted more interest for the purpose of improving the performance of permanent magnet materials[17] and combating the superparamagnetic limit for magnetic recording media.[18]

Over the past few decades, nanosized 3d-transition-metal oxides have been studied intensively due to their importance in fundamental research and diverse technical applications.[19] Nanoparticles of iron oxides such as magnetite (Fe_3O_4) and maghemite (γ-Fe_2O_3) have a wide range of applications in ferrofluids, magnetic storage media, targeted drug delivery, and magnetic resonance imaging (MRI), because of their chemical stability and excellent FM characteristics.[20,21] But for Fe_3O_4 and γ-Fe_2O_3, there is a big difference in the structure and magnetic properties.[22,23] The anomalous magnetic properties of 3d-transition-metal monoxide (*viz.* FeO, CoO, and NiO) nanoparticles have also been studied systematically based on their AFM nature.[13,24,25] Generally speaking, magnetic materials at the nanometer scale show a variety of unique magnetic phenomena which are extremely different from the corresponding bulk. Just because of this, magnetic nanomaterials have aroused significant interest since these properties can be advantageous for utilization in many applications. And among them, related to properties and applications are the size, shape and composition of materials. For a variety of magnetic nanoparticles, Cheon *et al.* studied the influence of nanoscaling

[a] *New Energy Technology Engineering Laboratory of Jiangsu Province, Research Center of Information Physics and School of Science, Nanjing University of Posts and Telecommunications, Nanjing 210023, P. R. China. E-mail: liyt@njupt.edu.cn*
[b] *National Laboratory of Solid State Microstructures, Nanjing University, Nanjing 210093, P. R. China. E-mail: wzhong@nju.edu.cn*
[c] *Zernike Institute for Advanced Materials, Faculty of Science and Engineering, University of Groningen, Groningen 9747 AG, The Netherlands*
[d] *College of Science, Henan University of Technology, Zhengzhou 450001, P. R. China*

† Electronic supplementary information (ESI) available. See DOI: 10.1039/c9cp01265f

laws on their fundamental magnetic properties such as the blocking temperature (T_b), spin life time (τ), magnetization (M), coercivity (H_C), and susceptibility (χ) in detail.[19] Obviously, these scaling relationships can be leveraged to regulate the magnetism. Therefore, we are aware that the crux of the realization of the excellent performance is the precise control of material's microstructure.

The Curie temperature (T_C) of the bulk is 858 K for Fe_3O_4 and 948 K for γ-Fe_2O_3, while the T_N of FeO, CoO and NiO is 198 K, 293 K, and 523 K, respectively.[26] Exchange bias exists in a system composed of FM and AFM substances, where the T_C of the former is higher than the T_N of the latter.[1,8] There are preliminary studies reported on the EB effect of FeO/Fe_3O_4,[27,28] CoO/γ-Fe_2O_3[29,30] and Fe_3O_4/CoO[31] core–shell nanostructures in the literature. Actually, for the possible combinations, the γ-Fe_2O_3/NiO core–shell system is the most promising due to its high T_N and excellent stability.

One of the methods to create the EB phenomenon is by using core–shell structures. In recent years, core–shell structures (nanocomposites, binary nanoparticles, and hierarchical nanostructures) with controllable microstructure have attracted special attention due to their unique properties.[32,33] For example, Xi *et al.* synthesized Fe_3O_4/WO_3 hierarchical core–shell nanostructures with enhanced photocatalytic properties, resulting from the synergistic effect between the Fe_3O_4 core and the hierarchical WO_3 shell.[34] Panagiotopoulos *et al.* reported a simple chemical procedure for the synthesis of hybrid binary nanoparticles and studied the EB phenomenon in FM/AFM γ-Fe_2O_3/CoO and reverse AFM/FM CoO/γ-Fe_2O_3 binary nanoparticle systems.[29] In our previous work we have prepared Ni–NiO nanocomposites which exhibit large EB and enhanced coercivity at 5 K, resulting from heterojunctions at the interfaces between FM Ni and AFM NiO.[35] NiO nanomaterials have been extensively studied in many fields including catalysis, lithium-ion batteries, supercapacitors, gas sensors, and adsorbents in water treatment due to their outstanding physical and chemical properties.[36–38] The γ-Fe_2O_3/NiO core–shell nanostructure is even more interesting because of the combination with γ-Fe_2O_3 nanomaterials, which show excellent magnetic performance. However, it remains a great challenge to improve the γ-Fe_2O_3/NiO materials for a better controlled microstructure and stability. To date, there have been a few in-depth studies on the influence of microstructures on the magnetic properties of γ-Fe_2O_3/NiO nanostructures. We envisaged that γ-Fe_2O_3/NiO nanostructures can be more widely used once the above relationship is delineated.

In this paper, a facile and reproducible process is used to synthesis γ-Fe_2O_3/NiO core–shell nanostructures. The microstructure can be controlled by tuning the calcination temperature of the intermediate (Fe_3O_4/$Ni(OH)_2$ core–shell structures). We focus on the effects of different microstructures on the magnetic properties at room temperature and 5 K, including the size effect, phase content and interface coupling effect. The magnetization (M), the EB field (H_E) and the coercivity (H_C) of the samples were analyzed in detail. The result reveals certain H_E and enhanced H_C values in γ-Fe_2O_3/NiO core–shell nanostructures.

Experimental section

1. Sample preparation

The samples employed in this study were prepared by the commonly used three-step method. Fig. 1 depicts the synthesis process of the hybrid γ-Fe_2O_3/NiO core–shell nanostructures, which mainly comprises the following three steps.

Step I: the solvothermal synthesis of the seed (Fe_3O_4 microspheres). Firstly, 0.811 g (5 mmol) of $FeCl_3$ solid was dissolved in 40 mL of ethylene glycol (EG) with constant stirring for 15 min at room temperature until a clear solution was obtained. Subsequently, 3.6 g of NaOAc and 1.0 g of polyethylene glycol (PEG 4000) were added with faster stirring for another 15 min. The clear solution was then transferred into a 100 mL Teflon-lined stainless-steel autoclave. Secondly, the autoclave was heated up to 200 °C and maintained at this temperature for 8 h. When the reactions were over, the mixture of the product was cooled down to room temperature, and the black precipitate was washed with absolute ethanol and dried at 80 °C, and thus the Fe_3O_4 microspheres were obtained.

Step II: the synthesis of the intermediate (Fe_3O_4/$Ni(OH)_2$ core–shell structures). Firstly, the mixture of $Ni(NO_3)_2{\cdot}6H_2O$ (1.163 g, 4 mmol), ethanol (28 mL) and EG (12 mL) was manually stirred for 15 min in a beaker. After the formation of a clear light green solution, 0.132 g (4/7 mmol) of Fe_3O_4 powder was dispersed in the solution and sonicated for 20 min. Then the mixed solution was transferred to the autoclave and maintained at 160 °C for 8 h. After the solvothermal reactions,

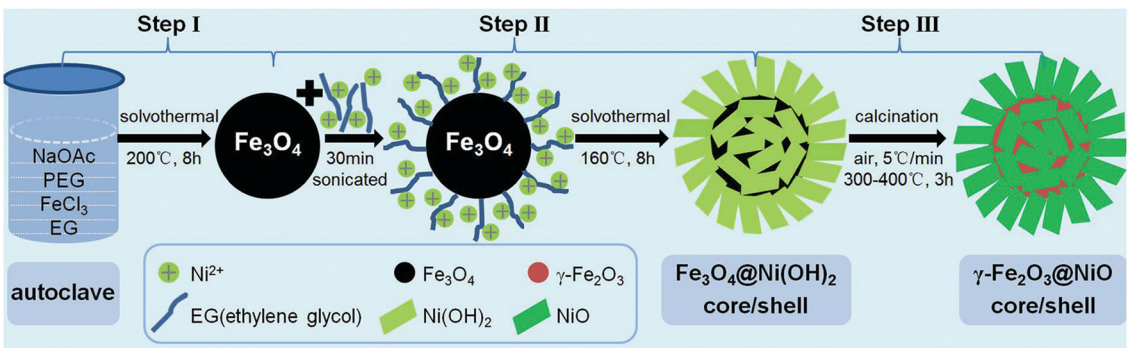

Fig. 1 Schematic illustration of the synthetic process for the hybrid γ-Fe_2O_3/NiO core–shell nanostructures.

Table 1 Results of the Rietveld analysis of the XRD patterns for the hybrid γ-Fe_2O_3/NiO core–shell nanostructures (samples M1–M3) formed at different calcination temperatures

		γ-Fe_2O_3 phase			NiO phase		
Sample	T (°C)	D (nm)	a (Å)	wt (%)	D (nm)	a (Å)	wt (%)
M1	300	17.1	8.3296	75.9	10.9	4.1759	24.1
M2	350	17.4	8.3463	58.9	11.2	4.2409	41.1
M3	400	18.2	8.3089	50.3	12.5	4.1709	49.7

the mixture was cooled down to room temperature, and the generated precipitate was washed using absolute ethanol. Finally, the product was dried in vacuum at 80 °C in an oven for 24 h, so that the products, Fe_3O_4/Ni(OH)$_2$ core–shell structures, were obtained.

Step III: the formation of the final product (γ-Fe_2O_3/NiO core–shell nanostructures). For the generation of the final product, the obtained intermediate (Fe_3O_4/Ni(OH)$_2$ core–shell structures) was heated at a speed of 5 °C min^{-1} at 300–400 °C and calcined in air at this temperature for 3 h. Ni(OH)$_2$ was transformed into NiO, and meanwhile, Fe_3O_4 was transformed into γ-Fe_2O_3 during this process. Consequently, three samples of γ-Fe_2O_3/NiO core–shell nanostructures denoted as M1, M2, and M3 in Table 1 were synthesized by controlling the calcination temperature, T.

2. Microstructural characterization

X-ray diffraction (XRD) patterns were determined using a Bruker D8 ADVANCE diffractometer with a Cu Kα radiation source (40 kV, 40 mA, λ = 1.54056 Å). Based on the information of the standard cards (γ-Fe_2O_3, $P4_132(213)$, a = 8.351 Å, JCPDS no. 39-1346; NiO, $Fm\bar{3}m(225)$, a = 4.178 Å, JCPDS no. 71-1179), the data from the XRD analysis were subsequently refined using the classical Rietveld method, and thus microstructural parameters such as the average crystallite size, the lattice parameter, and the phase content can be obtained. X-ray photoelectron spectroscopy (XPS) was performed using a Kratos Axis Ultra DLD spectrophotometer with an Al Kα radiation source. The Raman spectra of the samples were recorded in the range of 400–1600 cm^{-1}, using confocal Renishaw Invia at an excitation wavelength of 633 nm. The morphology of the sample was imaged with a Hitachi S-4800 scanning electron microscope (SEM) operating at an accelerating voltage of 5 kV. For transmission electron microscopy (TEM) studies, a drop of the tested powder sample in ethanol was deposited on each carbon-coated copper grid and then dried in air. Based on the Hitachi HT7700 instrument, high-resolution TEM (HRTEM) in conjunction with selected-area electron diffraction (SAED) analyses were used to determine the local microstructure.

3. Magnetic measurement

Using the MPMS-XL superconducting quantum interference device (SQUID), magnetic properties were recorded for powder samples in a gelatin capsule, and the magnetization M was measured against the magnetic field H and the temperature T. This part of measurements mainly included the following three aspects: (i) room-temperature (300 K) hysteresis (M–H) loops in a magnetic field up to 5000 Oe; (ii) low-temperature (5 K) M–H loops under zero-field-cooling (ZFC) and field-cooling (FC, from 330 K in a field of H_{cool} = 50 kOe); and (iii) ZFC and 500 Oe FC magnetization (M–T) curves in the temperature range of 2–330 K.

Results and discussion

To accurately investigate the structure and magnetic properties of the final product, we need to understand the microstructural characteristics of the seed and the intermediate first. Fig. 2 shows the relevant information of both parameters. The XRD pattern in Fig. 2(a) is obtained from seeds with a pure Fe_3O_4 structure. According to the Scherrer formula, the weak and wide diffraction peaks indicate that the grain size of Fe_3O_4 is in nanoscale. Correspondingly, Fig. 2(a1) shows the SEM image, indicating that the seeds have an Fe_3O_4 microsphere morphology, and the average size of these microspheres is about 0.4 μm. Because of the rough surface of the Fe_3O_4 microspheres, it is obvious that a gathering of smaller nanoparticles exists, agreeing with the XRD analysis.

The XRD pattern of the intermediate is shown in Fig. 2(b). Obviously, this pattern contains two sets of diffraction peaks, which correspond to Fe_3O_4 and Ni(OH)$_2$ phases, respectively. The diffraction peaks of Fe_3O_4 originate from the previous seed, while the two additional peaks (101) and (110) are in good agreement with those of α-Ni(OH)$_2$ packed with many sheets, which has already been reported by Liu *et al.* and Lee *et al.* and is stated in the standard card (JCPDS no. 14-0117).[39,40] The SEM image (Fig. 2(b1)) demonstrates that the Fe_3O_4–Ni(OH)$_2$ complex has a clear core–shell structure, where the Fe_3O_4 microspheres are cores and the Ni(OH)$_2$ nanosheets are shells. In conclusion, the intermediate is proven to be a Fe_3O_4/Ni(OH)$_2$ core–shell structure.

Based on the schematic illustration of the synthetic process shown in Fig. 1, we can deduce the formation mechanism of Fe_3O_4/Ni(OH)$_2$ core–shell nanostructures. Firstly, the Ni–glycolate complexes were easily attached onto the surface of the Fe_3O_4 microspheres by hydrogen bonding.[34,41] Secondly, these alcoholyzed Ni^{2+} ions were induced so that they aggregate and transform into Ni(OH)$_2$ nanocrystals supported on the Fe_3O_4 microspheres *via* hydrolyzation under solvothermal conditions (160 °C, 8 h).[42,43] Thirdly, well-packed nanosheets were formed on the surface of the Fe_3O_4 microspheres and through an alcoholysis reaction with Ni(OH)$_2$ nanocrystals working as the crystal seed. The final product was a Fe_3O_4/Ni(OH)$_2$ core–shell nanostructure.

Moreover, the Fe_3O_4/Ni(OH)$_2$ core–shell nanostructures were calcined at selected temperatures (300, 350 and 400 °C) for 3 h. To investigate the effect of the calcination temperature on the microstructure of the final product, the corresponding XRD patterns and SEM images were examined, as shown in Fig. 3. The crystalline nature and phase composition of the samples calcined at 300 °C, 350 °C and 400 °C were characterized by powder XRD, and the results are shown in Fig. 3(a)–(c), respectively. It is

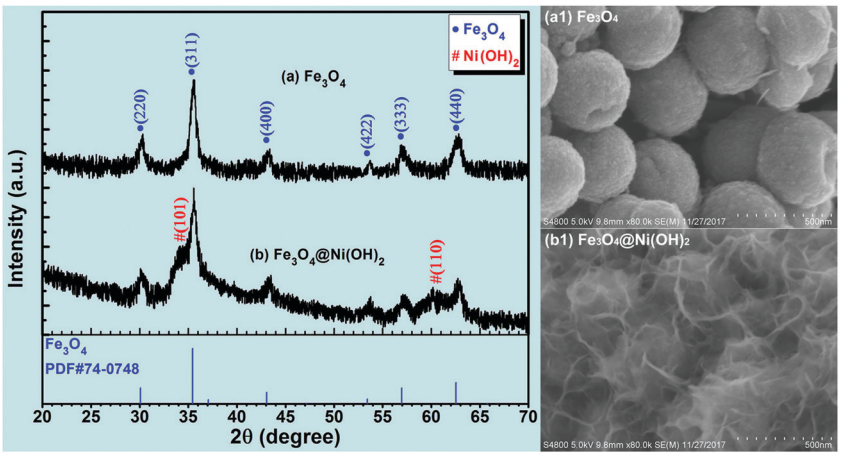

Fig. 2 XRD patterns of (a) the precursor Fe_3O_4 spheres and (b) the intermediate product Fe_3O_4/Ni(OH)$_2$ core–shell nanostructures; and (a1 and b1) are the corresponding SEM images.

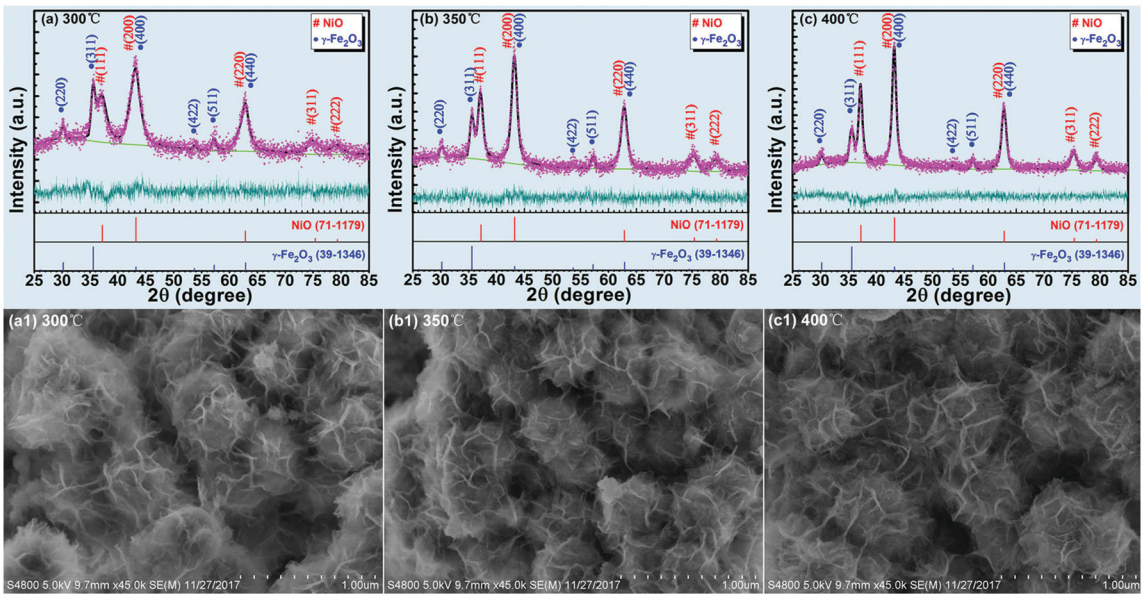

Fig. 3 XRD patterns showing the results of the Rietveld profile refinement for the hybrid γ-Fe_2O_3/NiO core–shell nanostructures formed at different calcination temperatures: (a) 300 °C, (b) 350 °C, and (c) 400 °C; (a1–c1) show the corresponding SEM images.

apparent that the positions of all the diffraction peaks which are marked with "#" match well with those of NiO (JCPDS no. 71-1179), and those marked with "●" agree with the standard XRD pattern of γ-Fe_2O_3 (JCPDS no. 39-1346).[44,45] No other crystalline impurities were detected in the XRD patterns. In other words, the obtained final product was exactly the γ-Fe_2O_3/NiO complex phase.

By comparing the XRD patterns of the samples calcined at 300 °C, 350 °C and 400 °C, it can be concluded that the broadening of the diffraction peaks becomes narrower and sharper as the calcination temperature increases, which indicates that the increase in the calcination temperature contributes to the improvement of crystallinity and the growth of grains. Moreover, the calcination temperature has a large effect on the phase content (wt%) of NiO or γ-Fe_2O_3. For example, the intensity ratio of the diffraction peaks $I_{NiO(111)}/I_{\gamma\text{-}Fe2O3(311)}$ changed from 0.83 to 2.24 as the calcination temperature increased from 300 °C to 400 °C, indicating that the content of NiO in the 400 °C-calcined sample was much higher than that in the 300 °C-calcined sample. Precisely, the microstructural parameters such as the average crystallite size (D), lattice parameter (a), and phase content (wt%) can be determined according to the Rietveld refinement. The results of the refinement are also shown in Fig. 3(a)–(c), and relevant data are listed in Table 1. All the quantitative results agree with the above analysis. In terms of magnetism, γ-Fe_2O_3 and NiO are categorized as FM and AFM materials, respectively.[46] Obviously, it makes a lot of difference for the magnetic properties of the above three samples. These assumptions are confirmed by the following magnetic analysis. It is the different calcination temperatures that lead to a change in the NiO content, accompanied by a growth in the grain size.

Furthermore, the morphology of the 300, 350 and 400 °C-calcined samples was investigated by SEM, as shown in Fig. 3(a1)–(c1). Obviously the samples were core–shell hierarchical structures. The previous Fe_3O_4 microspheres were further used as cores for the growth of NiO shells in order to obtain flower like γ-Fe_2O_3/NiO core–shell nanostructures. In particular, we can see that the NiO shells were composed of many irregular flake like nanosheets which were densely packed together on the surface of the γ-Fe_2O_3 microspheres. As the calcination temperature increases from 300 °C to 400 °C, the average size of the nanostructures increases, and the compactness of NiO shells is enhanced. The SEM analysis is consistent with the results of the XRD analysis.

Distinguishing the difference between magnetite (Fe_3O_4) and maghemite (γ-Fe_2O_3) is important for research on material performance, especially of their magnetic properties.[22,23] Undeniably, the XPS technique is a very effective method. In order to assess the chemical nature of the materials better, we recorded the XPS spectra of the Fe 2p and Ni 2p core level for all the synthesized samples, including the seed (Fe_3O_4), the intermediate (Fe_3O_4/$Ni(OH)_2$) and the final products (γ-Fe_2O_3/NiO-300 °C, γ-Fe_2O_3/NiO-350 °C and γ-Fe_2O_3/NiO-400 °C), as shown in Fig. S1 and S2 in the ESI.† Among them γ-Fe_2O_3/NiO-400 °C denotes the 400 °C-calcined sample, as a representative sample, and its XPS Fe 2p spectrum is displayed in Fig. 4(a). The photoelectron peaks with binding energies of about 711.0 eV and 722.1 eV are characteristic doublets for the Fe $2p_{3/2}$ and $2p_{1/2}$ spectra for iron oxides, respectively. The satellite peak at around 719.0 eV (see the inset) is the characteristic peak of γ-Fe_2O_3.[30,47–49] It is worth noting that the two XPS characteristic peaks associated with Fe 2p are present in all the five samples (see Fig. S1, ESI†), but the satellite peak corresponding to the γ-Fe_2O_3 only exists in three γ-Fe_2O_3/NiO core–shell nanostructure samples. As the calcination temperature decreases from 400 °C to 300 °C, the relative XPS intensity of the γ-Fe_2O_3 peak increases (see Fig. S1(c)–(e), ESI†), which is consistent with the phase analysis of XRD. In conclusion, the iron in the final product mainly exists in the form of γ-Fe_2O_3.

The XPS spectrum of the Ni 2p core level shown in Fig. 4(b) comprises four easily discernible features: the Ni $2p_{3/2}$ main peak and its satellite peak at about 854.1 eV and 860.2 eV and the Ni $2p_{1/2}$ main peak and its satellite peak at about 872.0 eV and 878.4 eV. This confirms the presence of the corresponding elements for the NiO nanoflake shell.[50] The XPS Ni 2p spectra of all the five samples are shown in Fig. S2 (see the ESI†). Eliminate the seed (Fe_3O_4), the other four samples (Fe_3O_4/$Ni(OH)_2$, γ-Fe_2O_3/NiO-300 °C, γ-Fe_2O_3/NiO-350 °C and γ-Fe_2O_3/NiO-400 °C) exhibit four distinct XPS peaks related to Ni 2p. As the calcination temperature increases from 300 °C to 400 °C, the intensity of the characteristic peak of the NiO component is slightly enhanced. Such a result corresponds to the discussions on XRD patterns and XPS Fe 2p spectra as well. Consequently, the existence of a typical γ-Fe_2O_3/NiO core–shell nanostructure was confirmed in the final products.

To further study the impact of the calcination temperature on the structure, the Raman spectra of the 300, 350, and 400 °C-calcined samples were characterized, as shown in Fig. 5. Among them, three peaks of the Raman-active mode were located at about 360.8 cm^{-1}, 491.5 cm^{-1} and 685.4 cm^{-1} for the γ-Fe_2O_3 component, which is close to the values reported in the literature.[51] Obviously, the calcination temperature had no impact on the Raman mode of the γ-Fe_2O_3 core. According to the previous XRD and SEM analysis, the microstructure of the γ-Fe_2O_3 core does not change much with calcination temperatures, which is consistent with the Raman mode. The Raman peak at 1400–1500 cm^{-1} corresponds to the active mode of the NiO component.[52] However, one important point is that the differences in the NiO shell (namely the orientation, size, thickness, compactness, *etc.*) significantly affected the Raman peak position of the three samples. The Raman peak of the NiO component shifts with the increasing calcination temperature, which is consistent with the above microstructural analysis.

For analyzing the influence of the calcination process, the Raman spectra of the seed (Fe_3O_4) and the intermediate (Fe_3O_4/$Ni(OH)_2$) were recorded as shown in Fig. S3 (see the ESI†). By comparing the characteristics of the Raman modes shown in

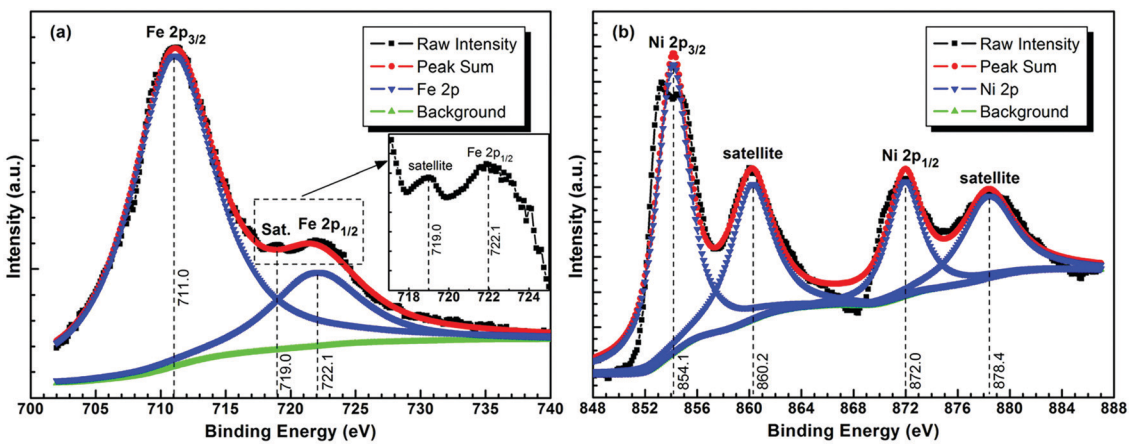

Fig. 4 XPS spectra of the (a) Fe 2p and (b) Ni 2p regions for the hybrid γ-Fe_2O_3/NiO core–shell nanostructures formed at 400 °C. Inset in panel (a) shows the details of the satellite peak.

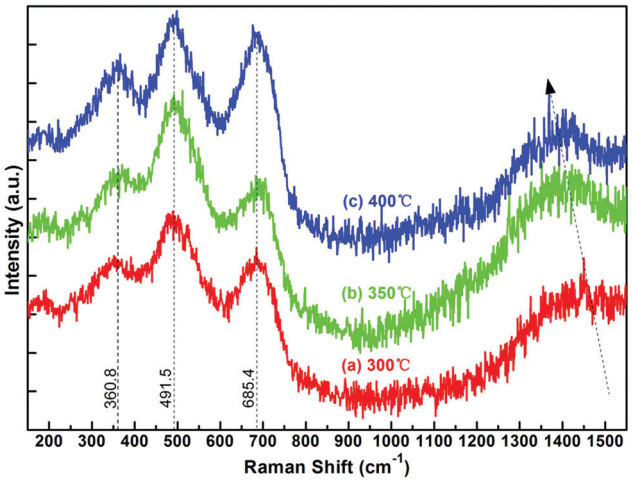

Fig. 5 Raman spectra of the hybrid γ-Fe_2O_3/NiO core–shell nanostructures formed at different calcination temperatures: (a) 300 °C, (b) 350 °C, and (c) 400 °C.

Fig. 5 and Fig. S3 (ESI†), it can be concluded that there are significant differences between the seed (Fe_3O_4) and the final product (γ-Fe_2O_3/NiO). The position, intensity and width of the Raman peaks change a lot among the seed, intermediate and final products, which indicate that during the two-step solvothermal and calcination processes, a fundamental shift occurs in terms of the chemical composition and microstructure of the products in each step, from Fe_3O_4 microspheres to Fe_3O_4/$Ni(OH)_2$ core–shell structures and then to γ-Fe_2O_3/NiO core–shell nanostructures. So far, the Raman spectra further confirm that the obtained final product is the γ-Fe_2O_3/NiO core–shell structure.

The microstructure, crystallinity and phase composition of γ-Fe_2O_3/NiO core–shell nanostructures were further explored by TEM, as shown in Fig. 6. As shown in Fig. 6(a)–(c), three samples formed at different calcination temperatures have the same core–shell structure. The deposition of shells can be clearly observed by the roughness and contrast, and the sizes of these core–shell nanostructures are relatively uniform. As the calcination temperature increased from 300 °C to 400 °C, the average diameter of γ-Fe_2O_3 cores and the average thickness of NiO shells increased slightly with an enhancement of the compactness of NiO shells. The SAED pattern shown in Fig. 6(d) indicates that the obtained samples have a structure of a composited phase. The hazy concentric circle corresponds to the polycrystalline γ-Fe_2O_3, and the dot matrix corresponds to the monocrystalline NiO. The anomaly, overlap and malposition of these bright spots were mainly caused by the disordered orientations of NiO nanosheets. According to the above TEM observations, both the structure and shape results are consistent with the results of XRD, XPS and SEM. Considering the fact that the samples are of good γ-Fe_2O_3–NiO interfaces, they will exhibit excellent magnetic properties.

Since the calcination temperature not only changes the phase content of γ-Fe_2O_3/NiO core–shell nanostructures but also has a large impact on the interface microstructure, the 300, 350 and 400 °C-calcined samples are very different in magnetic properties. Room-temperature (RT) hysteresis loops of the three

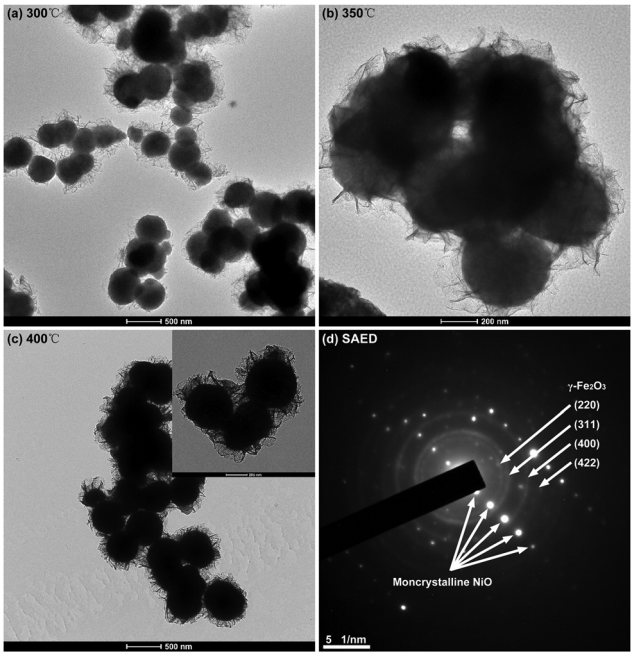

Fig. 6 TEM images of the hybrid γ-Fe_2O_3/NiO core–shell nanostructures formed at different calcination temperatures: (a) 300 °C, (b) 350 °C, and (c) 400 °C. The panel (d) shows the representative SAED pattern.

samples are shown in Fig. 7. The specific values of magnetic parameters such as the saturation magnetization M_s and the coercivity H_C of the three samples are listed in Table 2. Three samples formed at 300 °C, 350 °C and 400 °C, all exhibited strict FM behavior at RT, mainly because of the presence of the γ-Fe_2O_3 component in the three samples. In particular the 300 °C-calcined one displayed better FM properties, such as higher M_s and bigger H_C, due to the higher γ-Fe_2O_3 content or the lower NiO content in other words. The values of H_C at room temperature and M_s decrease with the increasing calcination temperature. The decreasing M_s is consistent with the XRD

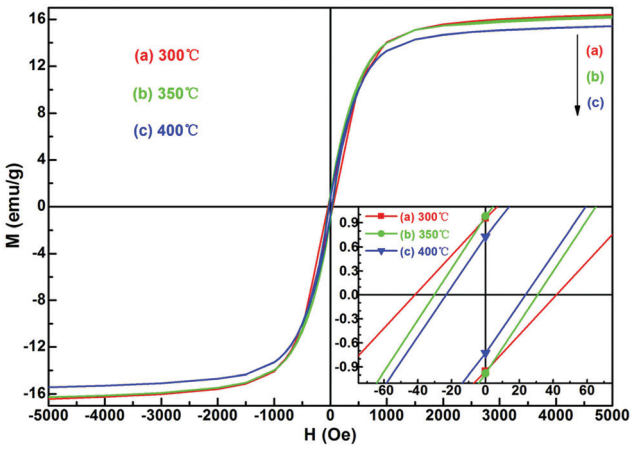

Fig. 7 RT (300 K) hysteresis loops of the hybrid γ-Fe_2O_3/NiO core–shell nanostructures formed at different calcination temperatures: (a) 300 °C, (b) 350 °C, and (c) 400 °C. Inset shows the details of the same loops around the origin.

Table 2 Magnetic parameters of the hybrid γ-Fe_2O_3/NiO core–shell nanostructures (samples M1–M3) formed at different calcination temperatures

		300 K		5 K				
Sample	T (°C)	M_s (emu g^{-1}) (±0.5)	H_C (Oe) (±2)	M_s (emu g^{-1}) (±0.5)	H_C (ZFC) (Oe) (±10)	H_C (FC) (Oe) (±10)	H_E (Oe) (±2)	ΔH_C (Oe) (±2)
M1	300	16.5	42	22.8	160	213	50	53
M2	350	16.3	31	20.6	146	206	52	60
M3	400	15.5	23	19.4	118	190	60	72

results; with the decreasing γ-Fe_2O_3 content the magnetization decreases. The values of RT coercivity is smaller than the corresponding values of the soft magnet, H_C = 125 Oe.[46] Moreover, Fig. S4 (see the ESI†) displays the RT hysteresis loop of the seed, Fe_3O_4 microspheres, as well. The values of M_s and H_C for the Fe_3O_4 microspheres are 47.4 emu g^{-1} and 23 Oe, respectively. Such a M_s value is very close to 480 kA m^{-1} of the bulk Fe_3O_4,[23] which is mainly due to the submicron size of the Fe_3O_4 microspheres. Compared to the γ-Fe_2O_3/NiO samples, Fe_3O_4 not only holds a higher saturation magnetization but is also smaller in coercivity, which ultimately causes the excellent soft-magnetic behavior of Fe_3O_4 microspheres. From the RT magnetic point of view, Fe_3O_4 is therefore different from γ-Fe_2O_3.

Field-cooling (FC) is necessary to induce an exchange anisotropy in hybrid FM–AFM systems. In order to measure the EB field, the three samples formed at 300 °C, 350 °C and 400 °C were cooled down from 330 K (below the T_N, 523 K for the bulk NiO) to 2 K in a magnetic field of 50 kOe. The magnetization M was then measured as a function of the magnetic field H at 5 K, and the obtained zero-field-cooling (ZFC) and FC loops are shown in Fig. 8. Both ZFC and FC loops revealed that the saturation magnetization (M_s = 22.8 ± 0.5 emu g^{-1}) for the 300 °C-calcined sample is higher than that (M_s = 19.4 ± 0.5 emu g^{-1}) for the 400 °C-calcined sample. This is mainly due to the higher γ-Fe_2O_3 (or lower NiO) content in the former. Furthermore, as listed in Table 2, the magnetization at 5 K is larger than that at RT due to the disappearance of thermal fluctuation at low temperature.[53,54] From RT to 5 K, the coercivity of the samples increases with decreasing temperature. Such coercivity enhancement most likely originates from the nanostructure nature of the samples.

At 5 K, the ZFC loops of the three samples formed at 300 °C, 350 °C and 400 °C reveal a relatively large coercivity (H_C(ZFC) = 160 Oe, 146 Oe and 118 Oe, respectively), mainly because of the γ-Fe_2O_3/NiO complex phase. Based on the above microstructure analysis, there are good γ-Fe_2O_3–NiO interfaces in this kind of composite nanostructures. The coupling interaction between the FM γ-Fe_2O_3 and AFM NiO components allows a variety of reversal paths for the spins upon cycling the applied field, and thereby resulting in a large coercivity.[25] The numerical difference between them mainly depends on the ratio of γ-Fe_2O_3 and NiO phases.

As for the FC loops, the EB field H_E is determined from the loop shift and calculated as $H_E = (H_{C1} - H_{C2})/2$, where H_{C1} and H_{C2} are the negative and positive coercive fields, respectively. For the three γ-Fe_2O_3/NiO samples, the FC loops differ from the ZFC loops (see the central region of the loops shown in Fig. 8). The ZFC loops are perfectly symmetric; however, horizontal shifts are observed in the FC hysteresis loops. This asymmetry proves the existence of exchange biased interfaces in the three samples. To be specific, the γ-Fe_2O_3/NiO samples formed at 300 °C, 350 °C and 400 °C display a certain EB (H_E = 50 Oe, 52 Oe and 60 Oe, respectively) because of the coupling interaction between the FM γ-Fe_2O_3 and AFM NiO components. The H_E change is correlated to the microstructural characteristics such as the size, phase content and interface roughness. Furthermore, such a coupling effect allows a variety of reversal paths for the spins upon cycling the applied field,[25] and thereby resulting in the enhancement of coercivity. By comparison, the difference of coercivity under FC and ZFC processes can be defined as $\Delta H_C = H_C(FC) - H_C(ZFC)$. The specific values of ΔH_C for the three γ-Fe_2O_3/NiO samples are listed in Table 2. For the 300 and 400 °C-calcined samples, the values of H_E and ΔH_C for the former are smaller than those for the latter, and the values are strongly influenced by the phase content of AFM NiO.

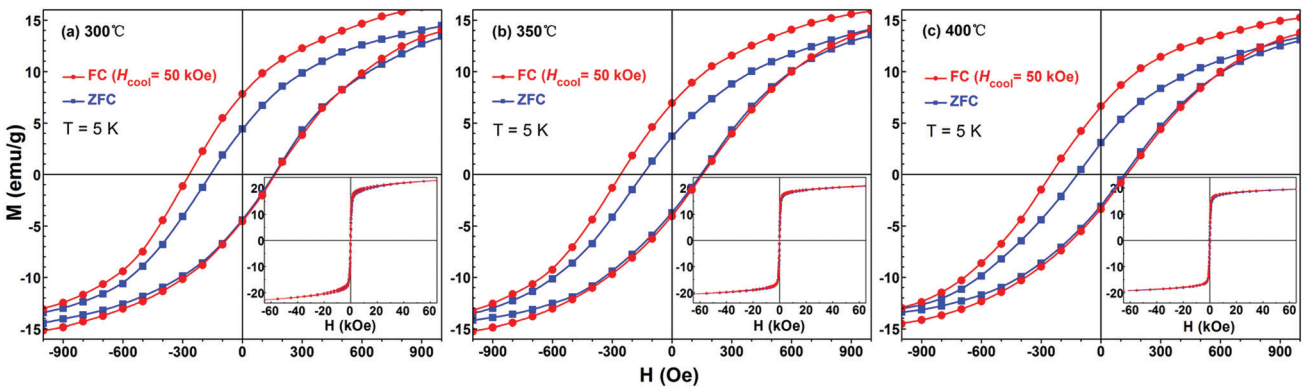

Fig. 8 ZFC and FC (from 330 K in a cooling field of 50 kOe) 5 K hysteresis loops of the hybrid γ-Fe_2O_3/NiO core–shell nanostructures formed at different calcination temperatures: (a) 300 °C, (b) 350 °C, and (c) 400 °C. The central region of the loops is shown, and the complete loops are shown in the insets.

This is because the NiO content of the 400 °C-calcined sample is much higher than that of the 300 °C-calcined one.

Compared to thousands oersted (Oe) of the H_E values exhibited by other EB-based systems such as Co/CoO,[13,14] CoO/γ-Fe_2O_3,[29,30] Fe_3O_4/CoO,[31] MnO/Mn_3O_4,[55,56] and FeO/Fe_3O_4[57] the value mentioned here is fairly small. The quality of the γ-Fe_2O_3–NiO interface itself (for example, the contact mode and the contact area) is one of the reasons. However, the main reason is the defect of the NiO nanosheet, for example, magnetocrystalline anisotropy or surface disorder. As reported by several authors,[58–60] nano-scaled NiO displays structural disorder at the surface which may result in random magnetic anisotropy and frustration of competing magnetic interactions in EB-based systems. Del Bianco *et al.*[58,61] reported that the magnetic behavior of the Ni/NiO system is ultimately determined by the anisotropy energy barrier distribution of the disordered NiO component. What's more, it has been reported that the NiO nanoparticles consist of magnetically and structurally ordered nanocrystallites and a disordered NiO component, with a glassy character, embodying net FM moments. Considering the present samples, flower like γ-Fe_2O_3/NiO core–shell nanostructures, the NiO shells are built of many irregular nanosheets which enclose the surface of the γ-Fe_2O_3 core, and the orientation of NiO nanosheets is disordered. Therefore, the partial magnetic behavior of the γ-Fe_2O_3/NiO samples at 5 K can be expected due to the disordered NiO magnetic component. In the FC magnetization, by decreasing the temperature, the FM moments progressively block, while the spins of the disordered NiO component are frozen in a spin-glass-like state. This factor eventually results in a small H_E and ΔH_C. As explained later, the temperature dependence of FC magnetization confirms this interpretation.

Fig. 9 shows the temperature dependence of the magnetization M of the three samples under both ZFC and FC conditions in a field of 500 Oe. There are differences in magnetic irreversibility between M_{FC} and M_{ZFC}. We observed an increase of M_{ZFC} and a decrease of M_{FC} with increasing temperature, and the variation of M_{ZFC} is much more obvious than that of the M_{FC}. In particular, at low temperatures, the FC magnetization is almost constant. Perhaps this corroborates the statement of the disordered NiO component we mentioned above. As can be seen from the ZFC/FC curves, the γ-Fe_2O_3 component remains FM up to the Néel temperature T_N of AFM NiO (although the T_N is not reflected in the ZFC curves), which indicates that an extra anisotropy is induced such that $K_UV \gg k_BT$,[13] where K_U is anisotropy, V is the magnetic volume, and k_B is the Boltzmann constant. In this case, the FM moments of γ-Fe_2O_3 are prevented from flipping over the energy barrier for all temperatures below the T_N of NiO, and thus the hybrid γ-Fe_2O_3/NiO core–shell nanostructures remain magnetically stable below this temperature. At low enough temperature, the AFM moments (*e.g.* NiO) are frozen in a spin-glass-like state. Once the temperature increases, the NiO regions start to unfreeze progressively. Once the net moments of NiO shells are subject to thermal fluctuation, they tend to be polarized by the moment of the γ-Fe_2O_3 core. This effect occurs when a magnetic field is applied, which benefits the formation of a FM network throughout the core–shell samples. One can assume that it is the polarization of FM components that results in the background rise of ZFC curves, which is in correspondence with the rising tendency of M_{ZFC}. Though, upon the restart of cooling, the FM moments remain locked in the direction of the external field, the change in M_{FC} is not as significant as that in M_{ZFC}. Furthermore, there is no maximum value observed in ZFC magnetization, implying a T_N higher than 330 K. For all three γ-Fe_2O_3/NiO samples, the splitting between ZFC and FC magnetization is observed in the whole temperature range up to 330 K. An analogous phenomenon was also reported in the Ni–NiO system.[35,62,63]

As reported in several studies,[62,64–66] the partial magnetic behavior of the FM/AFM systems containing NiO can be interpreted by considering a disordered NiO component. The FC curve shows that ferromagnetic moments are progressively blocked by the decreasing temperature, while spins of the disordered NiO component are frozen in a spin-glass-like state. Obviously, the temperature dependence of M_{FC} confirms this point. Furthermore, M_{FC} is almost a constant at low temperature. The insets in Fig. 9 show the temperature derivative of the difference between FC and ZFC magnetizations, $-d(M_{FC} - M_{ZFC})/dT$. Such a derivative curve provides quantitative information on the magnetic

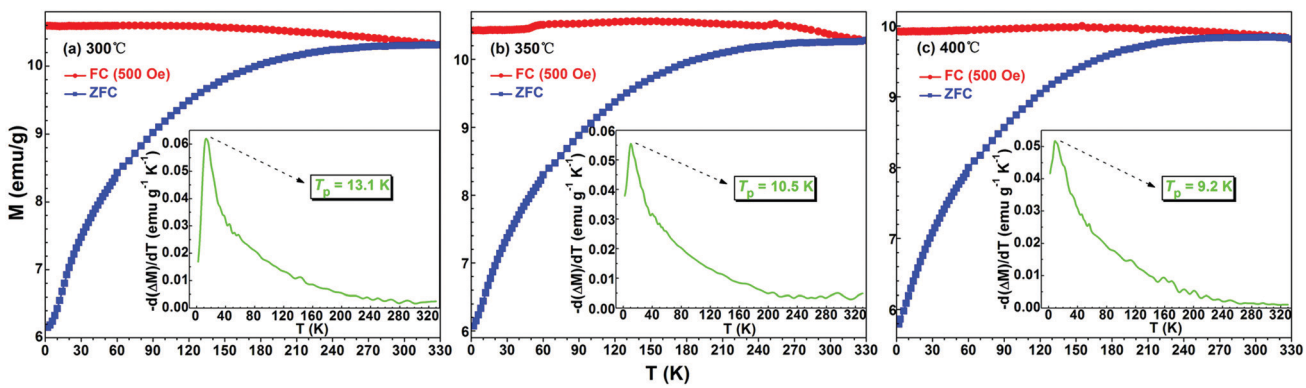

Fig. 9 ZFC and 500 Oe FC magnetization *vs.* temperature (M–T) curves of the hybrid γ-Fe_2O_3/NiO core–shell nanostructures formed at different calcination temperatures: (a) 300 °C, (b) 350 °C, and (c) 400 °C. Insets show the temperature derivative of the difference between the FC and ZFC magnetizations.

behaviors of the nanosystem.[67] The peak located at T_p indicates a frozen disordered magnetic state at low temperatures below this peak. The T_p values of the three samples formed at 300 °C, 350 °C and 400 °C are 13.1 K, 10.5 K and 9.2 K, respectively. In one word, the ferromagnetic moments are in a blocked state and a frozen magnetic state is formed at lower temperature. The differences in M and T_p between the three γ-Fe_2O_3/NiO samples are related to their microstructures such as the core–shell size, phase content, and interface characteristics. Analogous results are also observed in Fe/Fe-oxide[67] and Ni/NiO nanostructures.[58,62]

Conclusions

A microstructure-controlled preparation of hybrid γ-Fe_2O_3/NiO core–shell nanostructures has been carried out *via* a three-step method. The obtained powder samples were characterized by XRD, SEM, XPS, Raman, HRTEM, SAED and SQUID techniques. The results indicate that all of the samples are of distinct core–shell structures, where the γ-Fe_2O_3 microspheres are cores and the NiO nanosheets are shells. Flake like NiO nanosheets with chaotic orientation and a monocrystalline structure were packed together on the surface of the γ-Fe_2O_3 sphere. As the calcination temperature increased from 300 °C to 400 °C, the average size and NiO content of the samples increased, together with an enhancement of the compactness of NiO shells. The size effect, phase content of antiferromagnetic NiO, interface microstructure and FM–AFM coupling interaction have significant impacts on the magnetic properties of γ-Fe_2O_3/NiO core–shell nanostructures. The existence of exchange bias may have resulted from the coupling effect between FM γ-Fe_2O_3 and AFM NiO components. At the same time, such an exchange coupling effect allows a variety of reversal paths for the spins upon cycling the applied field, resulting in the enhancement of coercivity. Furthermore, the temperature dependence of magnetization for the hybrid γ-Fe_2O_3/NiO samples under ZFC/FC processes shows that an extra anisotropy was induced. Consequently, the γ-Fe_2O_3/NiO core–shell nanostructures exhibit certain exchange bias (H_E = 60 Oe) and enhanced coercivity (H_C = 213 Oe).

Conflicts of interest

There are no conflicts to declare.

Acknowledgements

We would like to thank Engineer Liya Lü of Nanomagnetism Research Group, Nanjing University for SQUID measurement. This work was financially supported by the National Natural Science Foundation (Grant No. 11604160, 11474151 and 11605092), the Natural Science Foundation of Jiangsu Province (Grant No. BK20160876), the Scientific Research Foundation of Nanjing University of Posts and Telecommunications (NUPTSF, Grant No. NY215063 and NY217096), and the Open Project for National Laboratory of Solid State Microstructures, Nanjing University (Grant No. M30007), P. R. China.

References

1 W. H. Meiklejohn and C. P. Bean, *Phys. Rev.*, 1956, **102**, 1413–1414.
2 A. E. Berkowitz and K. Takano, *J. Magn. Magn. Mater.*, 1999, **200**, 552–570.
3 J. Nogués and I. K. Schuller, *J. Magn. Magn. Mater.*, 1999, **192**, 203–232.
4 J. Cramer, F. Fuhrmann, U. Ritzmann, V. Gall, T. Niizeki, R. Ramos, Z. Y. Qiu, D. Z. Hou, T. Kikkawa, J. Sinova, U. Nowak, E. Saitoh and M. Kläui, *Nat. Commun.*, 2018, **9**, 1089.
5 C. Chappert, A. Fert and F. N. Van Dau, *Nat. Mater.*, 2007, **6**, 813–823.
6 T. Newhouse-Illige, Y. H. Liu, M. Xu, D. Reifsnyder Hickey, A. Kundu, H. Almasi, C. Bi, X. Wang, J. W. Freeland, D. J. Keavney, C. J. Sun, Y. H. Xu, M. Rosales, X. M. Cheng, S. F. Zhang, K. A. Mkhoyan and W. G. Wang, *Nat. Commun.*, 2017, **8**, 15232.
7 K. Akmaldinov, L. Frangou, C. Ducruet, C. Portemont, J. Pereira, I. Joumard, B. Dieny, J. Alvarez-Hérault and V. Baltz, *IEEE Magn. Lett.*, 2015, **6**, 3000404.
8 J. Nogués, J. Sort, V. Langlais, V. Skumryev, S. Suriñach, J. S. Muñoz and M. D. Baró, *Phys. Rep.*, 2005, **422**, 65–117.
9 A. Mougin, T. Mewes, M. Jung, D. Engel, A. Ehresmann, H. Schmoranzer, J. Fassbender and B. Hillebrands, *Phys. Rev. B: Condens. Matter Mater. Phys.*, 2001, **63**, 060409(R).
10 F. X. Redl, C. T. Black, G. C. Papaefthymiou, R. L. Sandstrom, M. Yin, H. Zeng, C. B. Murray and S. P. O'Brien, *J. Am. Chem. Soc.*, 2004, **126**, 14583–14599.
11 Z. M. Tian, S. L. Yuan, S. Y. Yin, L. Liu, J. H. He, H. N. Duan, P. Li and C. H. Wang, *Appl. Phys. Lett.*, 2008, **93**, 222505.
12 D. H. Zhang, Z. Q. Liu, S. Han, C. Li, B. Lei, M. P. Stewart, J. M. Tour and C. W. Zhou, *Nano Lett.*, 2004, **4**, 2151–2155.
13 V. Skumryev, S. Stoyanov, Y. Zhang, G. Hadjipanayis, D. Givord and J. Nogués, *Nature*, 2003, **423**, 850–853.
14 S. E. Inderhees, J. A. Borchers, K. S. Green, M. S. Kim, K. Sun, G. L. Strycker and M. C. Aronson, *Phys. Rev. Lett.*, 2008, **101**, 117202.
15 K. Nadeem, A. Ullah, M. Mushtaq, M. Kamran, S. S. Hussain and M. Mumtaz, *J. Magn. Magn. Mater.*, 2016, **417**, 6–10.
16 A. C. Gandhi and J. G. Lin, *J. Phys.: Condens. Matter*, 2017, **29**, 215802.
17 M. C. Spadaro, S. D'Addato, P. Luches, S. Valeri, V. Grillo, E. Rotunno, M. A. Roldan, S. J. Pennycook, A. M. Ferretti, E. Capetti and A. Ponti, *Nanotechnology*, 2015, **26**, 405704.
18 A. Roy, J. A. De Toro, V. S. Amaral, P. Muniz, J. M. Riveiro and J. M. F. Ferreira, *J. Appl. Phys.*, 2014, **115**, 073904.
19 Y.-W. Jun, J.-W. Seo and J. Cheon, *Acc. Chem. Res.*, 2008, **41**, 179–189.
20 A. H. Lu, E. L. Salabas and F. Schüth, *Angew. Chem., Int. Ed.*, 2007, **46**, 1222–1244.
21 R. Hao, R. J. Xing, Z. C. Xu, Y. L. Hou, S. Gao and S. H. Sun, *Adv. Mater.*, 2010, **22**, 2729–2742.
22 V. V. Osipov, V. V. Platonov, M. A. Uimin and A. V. Podkin, *Tech. Phys.*, 2012, **57**, 543–549.

23 A. P. Safronov, I. V. Beketov, S. V. Komogortsev, G. V. Kurlyandskaya, A. I. Medvedev, D. V. Leiman, A. Larrañaga and S. M. Bhagat, *AIP Adv.*, 2013, **3**, 052135.
24 Y. L. Hou, Z. C. Xu and S. H. Sun, *Angew. Chem.*, 2007, **119**, 6445–6448.
25 R. H. Kodama, S. A. Makhlouf and A. E. Berkowitz, *Phys. Rev. Lett.*, 1997, **79**, 1393–1396.
26 C. N. R. Rao and B. Raveau, *Transition Metal Oxides*, Wiley-VCH, Weinheim, 1995.
27 D. W. Kavich, J. H. Dickerson, S. V. Mahajan, S. A. Hasan and J.-H. Park, *Phys. Rev. B: Condens. Matter Mater. Phys.*, 2008, **78**, 174414.
28 X. L. Sun, N. F. Huls, A. Sigdel and S. H. Sun, *Nano Lett.*, 2012, **12**, 246–251.
29 I. Panagiotopoulos, G. Basina, V. Alexandrakis, E. Devlin, G. Hadjipanayis, L. Colak, D. Niarchos and V. Tzitzios, *J. Phys. Chem. C*, 2009, **113**, 14609–14614.
30 C. Liu, J. G. Cui, X. M. He and H. G. Shi, *J. Nanopart. Res.*, 2014, **16**, 2320.
31 W. Baaziz, B. P. Pichon, C. Lefevre, C. Ulhaq-Bouillet, J.-M. Greneche, M. Toumi, T. Mhiri and S. Bégin-Colin, *J. Phys. Chem. C*, 2013, **117**, 11436–11443.
32 J. Liu, S. Z. Qiao, S. B. Hartono and G. Q. Lu, *Angew. Chem., Int. Ed.*, 2010, **49**, 4981–4985.
33 E. V. Shevchenko, M. I. Bodnarchuk, M. V. Kovalenko, D. V. Talapin, R. K. Smith, S. Aloni, W. Heiss and A. P. Alivisatos, *Adv. Mater.*, 2008, **20**, 4323–4329.
34 G. C. Xi, B. Yue, J. Y. Cao and J. Ye, *Chem. – Eur. J.*, 2011, **17**, 5145–5154.
35 X. J. Yao, X. M. He, X. Y. Song, Q. Ding, Z. W. Li, W. Zhong, C.-T. Au and Y. W. Du, *Phys. Chem. Chem. Phys.*, 2014, **16**, 6925–6930.
36 B. Varghese, M. V. Reddy, Y. M. Zhu, C. S. Lit, T. C. Hoong, G. V. Subba Rao, B. V. R. Chowdari, A. T. S. Wee, C. T. Lim and C.-H. Sow, *Chem. Mater.*, 2008, **20**, 3360–3367.
37 Z. Song, L. F. Chen, J. C. Hu and R. Richards, *Nanotechnology*, 2009, **20**, 275707.
38 S. J. Ding, T. Zhu, J. S. Chen, Z. Wang, C. Yuan and X. W. Lou, *J. Mater. Chem.*, 2011, **21**, 6602–6606.
39 B. H. Liu, S. H. Yu, S. F. Chen and C. Y. Wu, *J. Phys. Chem. B*, 2006, **110**, 4039–4046.
40 J. W. Lee, J. M. Ko and J.-D. Kim, *J. Phys. Chem. C*, 2011, **115**, 19445–19454.
41 Y. Wang, S. K. Li, X. R. Xing, F. Huang, Y. Shen, A. Xie, X. Wang and J. Zhang, *Chem. – Eur. J.*, 2011, **17**, 4802–4808.
42 X. F. Song and L. Gao, *J. Am. Ceram. Soc.*, 2008, **91**, 4105–4108.
43 T. Zhu, J. S. Chen and X. W. Lou, *J. Phys. Chem. C*, 2012, **116**, 6873–6878.
44 H. Deng, X. L. Li, Q. Peng, X. Wang, J. Chen and Y. Li, *Angew. Chem., Int. Ed.*, 2005, **44**, 2782–2785.
45 L. S. Zhong, J. S. Hu, H. P. Liang, A. M. Cao, W. G. Song and L. J. Wan, *Adv. Mater.*, 2006, **18**, 2426–2431.
46 B. D. Cullity and C. D. Graham, *Introduction to Magnetic Materials*, IEEE Press, New Jersey, 2009.
47 X. W. Teng, D. Black, N. J. Watkins, Y. Gao and H. Yang, *Nano Lett.*, 2003, **3**, 261–264.
48 T. Yamashita and P. Hayes, *Appl. Surf. Sci.*, 2008, **254**, 2441–2449.
49 G. B. Sun, B. X. Dong, M. H. Cao, B. Wei and C. Hu, *Chem. Mater.*, 2011, **23**, 1587–1593.
50 M. A. Peck and M. A. Langell, *Chem. Mater.*, 2012, **24**, 4483–4490.
51 G. V. M. Jacintho, P. Corio and J. C. Rubim, *J. Electroanal. Chem.*, 2007, **603**, 27–34.
52 N. Mironova-Ulmane, A. Kuzmin, I. Sildos and M. Pärs, *Cent. Eur. J. Phys.*, 2011, **9**, 1096–1099.
53 D. P. Dutta, S. Garima, P. K. Manna, A. K. Tyagi and S. M. Yusuf, *Nanotechnology*, 2008, **19**, 245609.
54 H. T. Zhang and X. H. Chen, *Nanotechnology*, 2005, **16**, 2288–2294.
55 G. Salazar-Alvarez, J. Sort, S. Suriñach, M. D. Baró and J. Nogués, *J. Am. Chem. Soc.*, 2007, **129**, 9102–9108.
56 A. E. Berkowitz, G. F. Rodriguez, J. I. Hong, K. An, T. Hyeon, N. Agarwal, D. J. Smith and E. E. Fullerton, *Phys. Rev. B: Condens. Matter Mater. Phys.*, 2008, **77**, 024403.
57 S. K. Sharma, J. M. Vargas, K. R. Pirota, S. Kumar, C. G. Lee and M. Knobel, *J. Alloys Compd.*, 2011, **509**, 6414–6417.
58 L. Del Bianco, F. Boscherini, A. L. Fiorini, M. Tamisari, F. Spizzo, M. V. Antisari and E. Piscopiello, *Phys. Rev. B: Condens. Matter Mater. Phys.*, 2008, **77**, 094408.
59 M. Thakur, M. Patra, S. Majumdar and S. Giri, *J. Alloys Compd.*, 2009, **480**, 193–197.
60 E. Winkler, R. D. Zysler, M. Vasquez Mansilla, D. Fiorani, D. Rinaldi, M. Vasilakaki and K. N. Trohidou, *Nanotechnology*, 2008, **19**, 185702.
61 L. Del Bianco, F. Boscherini, M. Tamisari, F. Spizzo, M. Vittori Antisari and E. Piscopiello, *J. Phys. D: Appl. Phys.*, 2008, **41**, 134008.
62 H. Ahmadvand, H. Salamati, P. Kameli and F. S. Razavi, *J. Supercond. Novel Magn.*, 2010, **23**, 1467–1471.
63 S. K. Sharma, J. M. Vargas, M. Knobel, K. R. Pirota, C. T. Meneses, S. Kumar, C. G. Lee, P. G. Pagliuso and C. Rettori, *J. Appl. Phys.*, 2010, **107**, 09D725.
64 A. C. Johnston-Peck, J. W. Wang and J. B. Tracy, *ACS Nano*, 2009, **3**, 1077–1084.
65 L. Del Bianco, F. Spizzo, M. Tamisari and A. Castiglioni, *J. Appl. Phys.*, 2011, **110**, 043922.
66 A. Querejeta-Fernández, M. Parras, A. Varela, F. del Monte, M. García-Hernández and J. M. González-Calbet, *Chem. Mater.*, 2010, **22**, 6529–6541.
67 L. Del Bianco, D. Fiorani, A. M. Testa, E. Bonetti, L. Savini and S. Signoretti, *Phys. Rev. B: Condens. Matter Mater. Phys.*, 2002, **66**, 174418.

